JMEPEG (2016) 25:3960–3971
DOI: 10.1007/s11665-016-2254-6

1059-9495/$19.00

Deformation Mechanism and Microstructure Evolution of T92/S30432 Dissimilar Welded Joint During Creep

Lianyong Xu, Yongfa Wang, Hongyang Jing, Lei Zhao, and Yongdian Han

(Submitted April 9, 2016; in revised form July 7, 2016; published online July 29, 2016)

The cross dissimilar welds between T92 martensitic steel and S30432 austenitic steel were crept at 625 °C with different applied stresses, and the creep deformation and microstructure behaviors were characterized. The results revealed that the creep deformation behavior of dissimilar weld joint was controlled by its martensitic T92 part due to the Ni-based filler metal employed. The fracture positions of crept dissimilar welded joints were located in base metal of T92 steel as the applied stress over than 140 MPa. The fracture type was mainly caused by plastic deformation and characterized by dimples and surface necking. In contrast, as applied stress was <140 MPa, fractured location was transferred into the fine-grained heat-affected zone of T92 part identified to be the intergranular brittle fracture. This phenomenon was controlled by creep deformation and related to undissolved carbides, fine grain size and constraint effect induced by creep deformation inconsistent in this zone.

Keywords creep rupture, deformation mechanism, dissimilar welded joint, failure transition

1. Introduction

Ultra-supercritical (USC) power plant whose steam temperature is up to 600 °C and pressure exceeds 27 MPa, has been generally accepted as a clean and high-efficiency thermal power generation technology and widely constructed around the world for the aim of dealing with energy shortage and environmental pollution (Ref 1-5). With the steam parameter increasing, the higher requirement for the materials applied in the USC plants must be available, such as good mechanical properties, high corrosion resistance, good fabricability and in particular high creep strength, which is the most important property for high-temperature and high-pressure components. This has led to the developments and applications of new heat-resistant alloys with the improvement of creep strength in recent years (Ref 3, 6). In order to fulfill the tough running parameters of the USC units, traditional heat-resistant steels used in the subcritical and some supercritical units are not suitable to the USC units any longer and have been replaced by those new heat-resistant steels, such as martensitic T92 (Ref 7-10) and austenitic S30432 steels (Ref 11-14).

To meet various property requirements and assure the economical construction of the boiler, different grades of steels are employed according to the service parameters. Although the martensitic steel can provide the higher creep rupture strength, its application temperature is limited to about 620 °C due to their corrosion resistance in high-temperature steam. Therefore, it is necessary to use austenitic steels for the boiler superheater and reheater tubes that experience higher temperatures (Ref 15, 16). Thus, martensitic/austenitic dissimilar welds are vital in boilers to join different metals together. In recent years, the welding techniques, the residual stress and the microstructures and mechanical properties of martensitic/austenitic dissimilar welds have been studied. Cao et al. (Ref 7) have implemented the T92/S30432 dissimilar steel welding through a gas tungsten arc welding (GTAW) technique using ERNiCr-3 welding wires and investigated the mechanical properties of the dissimilar welded joint. Chen et al. (Ref 17) have fabricated T92/S30432 dissimilar weld joint through a GTAW technique using a Ni-based welding wire of ERNiCrMo-3 and paid attention to the mechanical properties of the welds after aging at 650 °C. Zhao et al. (Ref 18) have investigated the residual stress distribution across the T92/S30432 dissimilar welded joint and obtained the measurements to reduce the residual stress level.

In addition to dealing with how to join these new martensite and austenite tube steels together and the strength of the dissimilar welds, for the dissimilar welded joints under high temperature, it is crucial to determine the reliabilities of these weld joints when they service tens of thousands of hours under the tough conditions of the USC units. Statistical analyses of cracking and failures of heavy tube size joints in British Central Electricity Generating Board (CEGB) plants operated over the last 20 years have shown that the failure and cracking incidence of dissimilar welds are one or two orders of magnitude greater than ferritic/ferritic welded joints (Ref 19). Furthermore, many researches have indicated that the creep resistance of dissimilar welded joints is deteriorated compared with the corresponding base materials (BMs). The creep behavior is the dominant key to the failures of dissimilar materials joints at elevated temperature. This has resulted in ongoing research activities placing emphasis on the creep properties and mechanism of the dissimilar welded joint, which found that creep rupture behavior of dissimilar welded joints under a range of stress showed different types (Ref 20-23). However, the literature information on the transition behavior and mechanism of T92 and S30432 dissimilar welded joint during crept under different stresses is rather limited. Therefore, the aim of present work is

Lianyong Xu, Yongfa Wang, Hongyang Jing, Lei Zhao, and **Yongdian Han**, School of Materials Science and Engineering, Tianjin University, Tianjin 300072, China; and Tianjin Key Laboratory of Advanced Joining Technology, Tianjin 300072, China. Contact e-mail: zhaolei85@tju.edu.cn.

to investigate the creep rupture behavior of T92 and S30432 dissimilar welded joint and then reveal the microstructure evolution and fracture characteristic of the dissimilar T92/S30432 martensitic/austenitic welded joint.

2. Experimental Procedures

2.1 Materials and Welding Procedure

The dissimilar welded tubes (an outer diameter of 52 mm, a wall thickness of 9.2 mm) made of martensitic T92 and austenitic S30432 BMs were produced through a multilayer GTAW method. The schematic of dissimilar welded joint is shown in Fig. 1, where a single-V-groove butt joint configuration with 70° groove angle and a root face of 1 mm is employed. The Ni-based filler metal, ERNiCr-3 (corresponding to INCONEL 82/182), was selected to join these metals. The welding parameters were: welding current in a range from 100 to 120 A, voltage from 8 to 9 V, traveling speed of 0.6 mm/s and electrode diameter of 1.6 mm. The chemical compositions for base metals and consumables are listed in Table 1, which are in accordance with the requirements of ASME SA-213 T92 and S30432 specifications, and ASME SFA-5.14 (AWS) specifications, respectively. After the welding, the welded joints were subjected to the post-weld heat treatment (PWHT) at 760 °C for 2 h in order to relieve residual stresses and stabilize the microstructure.

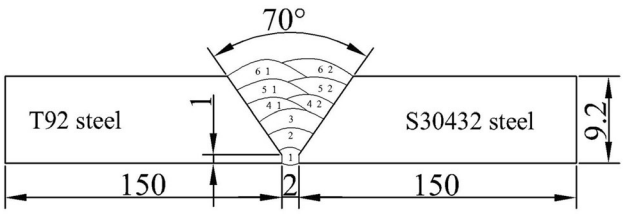

Fig. 1 Schematic of welding process for T92/S30432 dissimilar welded joints

2.2 Test Methods

The room temperature tensile properties of the joints were carried out using the sheet tension samples of 9.2 mm × 12 mm × 185 mm on the basis of ASTM E8/E8 M-15a. The load was applied by controlling the strain rate at 0.5 min^{-1}.

Cross-weld hardness measurements were taken using Vickers technique on the etched plain surfaces of prepared metallographic cross sections. All the hardness value was obtained along the centerline across the welded joint.

According to ASTM E139-11, the tensile cross-weld creep tests of the T92/S30432 dissimilar welded joints were conducted in air under a series of stresses from 180 to 110 MPa. The cylindrical tensile samples were employed and machined with the longitudinal axis parallel to the welded pipes axis. The gauge length of specimens was centered on the weld. The dimension and size of the employed specimen are shown in Fig. 2. All the creep tests were carried out in a lever arm constant load creep testing machine equipped with three-zone temperature control electric furnace. The test temperatures were kept at a specified temperature 625 °C and were controlled within ±1 °C.

After test, the microstructures and the fractographs of the creep specimens were observed using Olympus BX 53 light microscopy (LM) and Hitachi SU1510 scanning electron microscopy (SEM), respectively. For LM and SEM observations, the samples were ground (up to 2000 grit), polished (diamond paste) and etched. For the etching of dissimilar materials, different etching solutions were used, which are shown in Table 2.

Table 2 Etching solutions employed for T92/S30432 dissimilar welded joint

Materials	Composition of etching solution
Welded metal	Picric acid 5 g, ethanol 40 mL and H_2O 40 mL
ASME SA-213 T92	$FeCl_3$ 10 g, HCl 40 mL and H_2O 40 mL
ASME SA-213 S30432	$CuSO_4$ 8 g, HCl 40 mL and ethanol 40 mL

Table 1 Composition of employed base metals and consumables (wt.%)

Materials	C	Mn	P	S	Si	Cr	Mo	W	Ni	Nb	N	Cu	Ti	Al	B
T92	0.10	0.57	0.020	0.005	0.23	8.75	0.41	1.52	0.16	0.052	0.064	0.11	…	0.011	0.0024
S30432	0.089	0.61	0.022	0.005	0.26	18.47	…	…	8.97	0.44	0.085	3.01	…	0.011	0.0033
ERNiCr-3	0.034	3.05	0.001	0.002	0.11	20.19	…	…	71.50	2.52	…	0.022	0.36	…	…

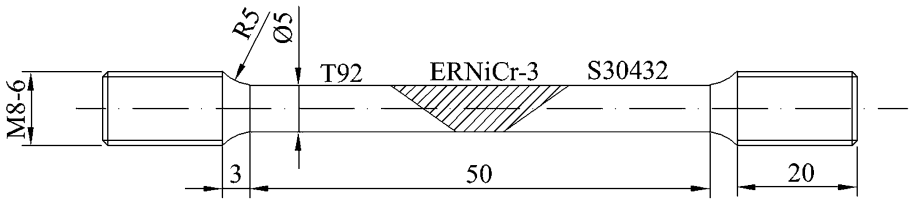

Fig. 2 Dimension and size of employed tensile cross-weld creep specimen

3. Results and Discussion

3.1 Mechanical Properties of the Dissimilar Welded Joints

The mechanical strength at room temperature of T92/S30432 dissimilar welded joint is shown in Table 3. It can be observed that the dissimilar welded joint exhibits qualified tensile strength. In addition, the fracture position of the joints is located in S30432 base metal, due to lower tensile strength of S30432 steel compared with T92 steel. The hardness distribution across the centerline of dissimilar welded joint is shown in Fig. 3. The interval between two hardness measurement points is fixed at 1 mm. It reveals that the weld seam is the low-hardness part. The hardness values near the fusion zones of HAZs increase to the peak point and then decrease gradually at a distance away from the fusion zone. The average value of hardness in the T92 side is expected to be larger than that in S30432 side regardless of the tested location, which is consistent with the corresponding strength shown in Table 3.

3.2 Microstructures Across the Dissimilar Welded Joint

It is well known that a dissimilar welded joint is often approximately divided into five regions, i.e., BM A, heat-affected zone (HAZ) of A, welded metal (WM), HAZ of B and BM B. LM microstructures of different regions in the as-received martensitic/austenitic welded joint after PWHT are shown in Fig. 4a-f for understanding the microstructure evolution of the dissimilar welded joint. Typical tempered martensite lath structure is shown in BM of T92 steel that is unaffected by welding, and the precipitated carbides from the matrix are distributed around the lath boundaries during the heat treatment (see Fig. 4a). The HAZ of T92 steel typically consists of fine-grained heat-affected zone (FGHAZ) and coarse-grained heat-affected zone (CGHAZ) subregions as a result of phase transformations taking place during the welding thermal cycle (Ref 24), which are shown in Fig. 4(b) and (c), respectively. It can be noted that in the HAZ of T92 steel, the martensite lath decomposes and the grain boundaries become vague. In addition, the grain size of FGHAZ is small compared with BM and CGHAZ. Because FGHAZ is next to BM of T92 steel, which is far away from the welding seam during welding compared with CGHAZ adjacent to the WM. As a result, the peak temperature of FGHAZ in welding thermal cycle is lower than that of CGHAZ, which leads to the non-completed austenitizing and inhibits the grain growth (Ref 17). The microstructure of Ni-based WM as shown in Fig. 4d is coarse cystiform-dendritic austenite, and the second phases are mainly diffuse distributed in the grain. Fully recrystallized polygonal austenitic grains with intergranular precipitates and twins are both observed in HAZ and BM on S30432 side, as shown in Fig. 4(e) and (f). Since S30432 steel does not undergo ferrite phase transformation during cooling, there are no HAZ subregions developed as they are known in martensitic steels (Ref 10). Furthermore, the grain size of HAZ in S30432 side is larger than that of BM. This is due to that the temperature in the HAZ of S30432 side is higher induced by the welding thermal cycle, resulting in the remarkable growth of the austenite grains.

Table 3 Tensile properties of T92/S30432 dissimilar welded joint at room temperature

σ_m (MPa)	δ (%)	Fracture position
Experiment		
701.25	40	BM of S30432
694.67	38	BM of S30432
700.29	38	BM of S30432
ASME SA-213 T92		
≥ 620	≥ 20	…
ASME SA-213 S30432		
≥ 590	≥ 35	…

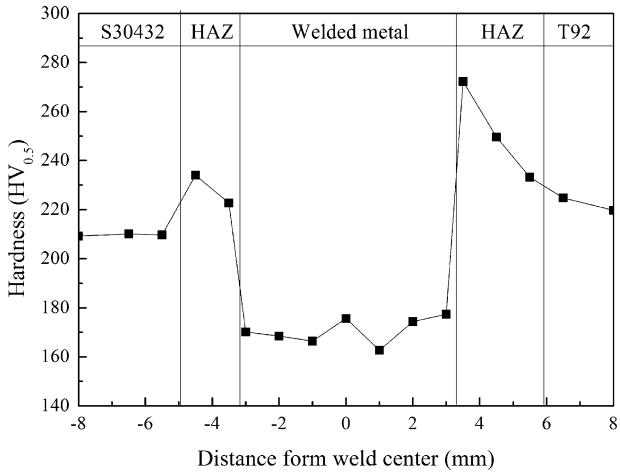

Fig. 3 Hardness distribution across centerline of T92/S30432 dissimilar materials joint

3.3 Creep Properties of the Dissimilar Welded Joints

Table 4 lists the creep rupture test results under load stresses ranging from 180 to 110 MPa at 625 °C for the T92/S30432 dissimilar welded joint. It can be seen that with the decrease in stress, the creep rupture time increases. In addition, the fracture position is mainly located in the T92 side, which can be ascribed to a relative low creep strength compared with S30432 steel and Ni-based WM. Furthermore, the fracture positions of the crept dissimilar welded joints are in BM on T92 side as the applied stress over than 140 MPa. After the joints crept for longer time, the joints fail in FGHAZ of T92 steel, which is known as Type IV cracking failure (Ref 25). This phenomenon is discussed in detail later.

In addition, the creep rupture strength versus the Larson-Miller parameter for T92/S30432 dissimilar welded joint at 625 °C is shown in Fig. 5. The 10^5 h creep rupture strength that is predicted from the Larson-Miller parameter is about 40 MPa. More experimental tests are necessary to accurately predict the long-time creep rupture strength.

3.4 Fracture Morphologies of Creep-Ruptured Specimens

Figure 6a-j, respectively, provides the fracture morphologies of crept specimen with different applied stresses. As shown in Fig. 6a, the surface concentration on the fracture surface of specimen crept at 180 MPa is very significant, which is about 20%, while the surface concentration gradually decreases as the applied stress decreases by comparing the fracture surfaces with different stresses. For the specimen crept at 110 MPa, there is

little necking and the fracture surface becomes more smooth in comparison with that at high stress (shown in Fig. 6i).

Besides, when the applied stress is above than 140 MPa, a typical dimple morphology can be clearly observed, meaning the ductility facture. This reveals that the plastic deformation is dominant. Some dimples gather together and even form the microcracks (Fig. 6d). It is interested to find that some spherical particles are observed in the dimples (Fig. 6b and d). These spherical particles may be formed by the hard second particles such as the carbides and carbonitrides precipitated during the creep deformation. The strength and hardness of the secondary particles are higher than that of the matrix. As a result, the

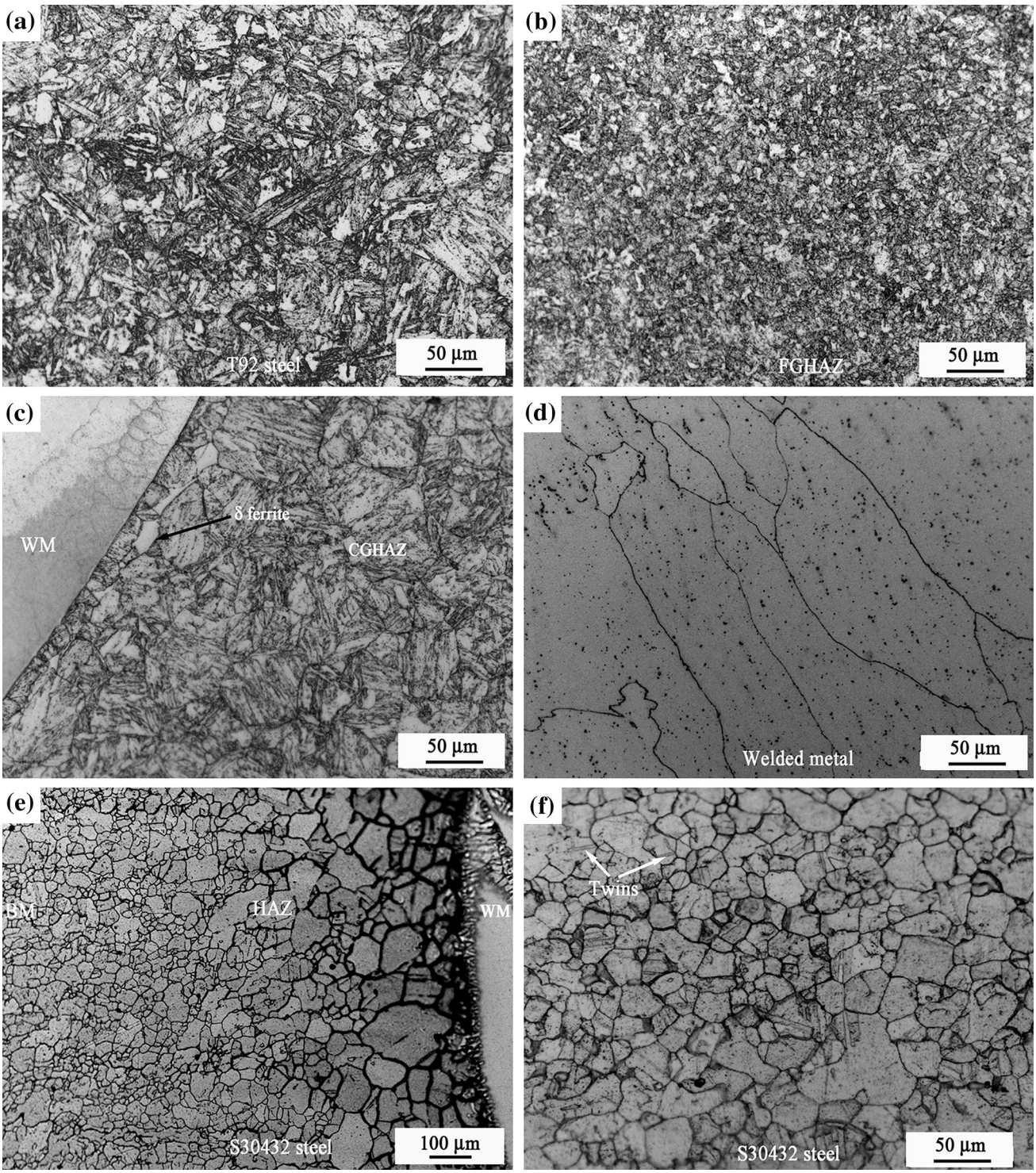

Fig. 4 Microstructures of different distinct regions across T92/S30432 welded joint: (a) T92 BM, (b) FGHAZ, (c) CGHAZ, (d) WM, (e) HAZ of S30432 and (f) S30432 BM

Table 4 Creep rupture test results of T92/S30432 dissimilar steels welded joints

Applied stress (MPa)	Fracture time (h)	Fracture position
T92/S30432 joint		
180	94	BM of T92
160	317	BM of T92
140	1433	FGHAZ of T92
120	2125	FGHAZ of T92
110	3737	FGHAZ of T92

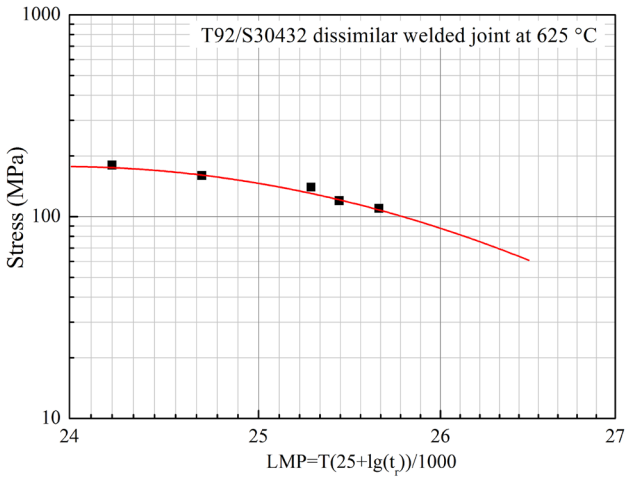

Fig. 5 Relation between creep rupture strength and creep rupture time curves for T92/S30432 dissimilar welded joint at 625 °C

deformation between secondary particles and matrix is inconsistent, which in turn leads to the formation of the microcracks. Thus, the effective net section area of the matrix is reduced and the surface is gradually contracted. The dimples are formed finally as the necking is too large to fail. But the secondary particles still remained in the dimples. These phenomena reveal that the fracture mechanism under high stress may be caused by the formation of the dimples. With the creep time increasing, the dimples grow and the adjacent dimples are linked to form the microcracks. In contrast, with the reduction in the applied stress, the dimples in fracture surfaces gradually decrease in size and number (see Fig. 6c-f) and even disappear (see Fig. 6g-j). The fracture mechanism is changed into the typical intergranular brittle fracture morphologies of Type IV cracking model (Ref 24, 26), which represents that the creep deformation is dominant rather than the plastic deformation.

3.5 Microstructure Evolution and Fracture Position in Dissimilar Welded Joint

Figure 7 shows the variation of microstructure appearances on the fracture positions in specimens crept at different stresses. It can be observed that similar voids occur as the applied stress changes. However, the size of voids under stress higher than 140 MPa is large, and lots of microcracks with large size are observed. In contrast, as the stress is <140 MPa, the occurred voids are small and the size of the formed microcracks is comparably small. On the basis of observed fracture morphologies in creep-ruptured specimens, it can be induced that the voids in the crept specimens with stress above than 140 MPa are mainly caused by the plastic deformation, while these in the crept specimens with stress lower than 140 MPa are mainly microcreep voids, which are consistent with SEM results. When the applied stress is <140 MPa, T92/S30432 dissimilar welded joints fail in FGHAZ on T92 side, the microstructure evolution of which during crept in the stress range of 180 to 110 MPa is shown in Fig. 8. It can be noted that as the stress over than 140 MPa, FGHAZ exhibits a good microstructure stability at high temperature, where there are few microvoids occurred (see Fig. 8a and b). As the applied stress decreases, the grains gradually decompose. In addition, the number of precipitated second phases which are distributed at grain and subgrain boundaries increases, and the size of these becomes large. These precipitates are mainly intergranular $M_{23}C_6$ (M = Cr, Fe) carbides and the intragranular MX (M = V, Nb; X = N, C) carbonitrides and precipitated from the lath martensite and the prior austenite grain boundary (Ref 24, 27). These have great effect on the creep deformation of the dissimilar welded joints. Firstly, the second particles in creeping solids influence the creep rate due to their interaction with free dislocation arrangements such as subgrain boundaries. Thus, creep rupture life strongly depends on the microstructural features of the particle population. Secondly, creep voids are apt to nucleate near these coarse precipitates and stimulate the creep deformation. As a result, the creep property of FGHAZ deteriorates most greatly among the dissimilar welded joint.

3.6 Creep Fracture Mechanism Analysis

Dissimilar martensitic/austenitic steels welded joint is apt to fail before the designed life. This is due to the formation of soft carbon-depleted zone at the martensitic side of the weld metal interface and the carbon migration from martensitic steel to austenitic weld metal, driven by carbon activity gradient (Ref 19, 28). The element distribution across the interface between HAZ of T92 and Ni-based WM is shown in Fig. 9. There are no abrupt chemical composition changes across the martensitic/authentic interface. This may be caused by the introduction of Ni-based welding consumables. Ni-based WM can act like a carbon diffusion barrier and suppress the carbon depletion at the martensitic side of the weld metal interface, due to the low carbon solubility of Ni-based filler materials (Ref 29). So, there is no soft creep zone present in T92/S30432 dissimilar joint. Although the mechanical strength of austenite steel at room temperature is lower than that of ferritic steel, the strength of ferritic steels at elevated temperatures is often not as high as that of austenitic stainless steels. Thus, T92/S30432 dissimilar welded joint is still apt to fracture at T92 side.

For T92/S30432 dissimilar welded joint crept under high stress, the plastic deformation is more dominant than the creep deformation, which is mainly caused by the grain boundary sliding. However, the sliding is apt to be hindered at the location of triple grain boundaries; thus, a high stress intensity is generated to stimulate the vacancy clustering. The dimples are always formed by the coalescence of the vacancies. With the growth and coalescence of the dimples, the fracture occurs.

As the stress decreases, the creep deformation becomes dominant. For T92 steel crept under low stress and high temperature, the grain boundary sliding is hard to achieve due to the reduction in the activation energy induced by a low stress. The voids are mainly formed by the diffusion of the

vacancy. Figure 10 shows the SEM microstructure of FGHAZ in the specimen crept at 110 MPa. It can be observed that the creep voids are mainly located at the grain boundaries and near the coarse precipitates (see Fig. 10b). For T92 steel, new coarsened second phase particles known as Laves phase are precipitated on the grain boundaries and the original $M_{23}C_6$ are also apt to coarsen during creeping (Ref 9, 24). Thus, the grain boundary sliding under the low stress is inhibited, which lead to a high concentration. These phenomena are all likely to be beneficial to the nucleation of the creep voids. For one thing, the creep voids are apt to nucleate near the coarse second phases (Ref 29). For another, a high concentration would stimulate the vacancy diffusion, which result in the nucleation of the creep voids (Ref 30). Then, with the creep time increasing, the vacancy would continuously migrate into the creep voids and make the creep voids grow. When the creep voids orient and coalesce to a certain extent, microcracks emerge.

This premature creep failure type typically occurs in FGHAZ region rather than BM as the applied stress decreases.

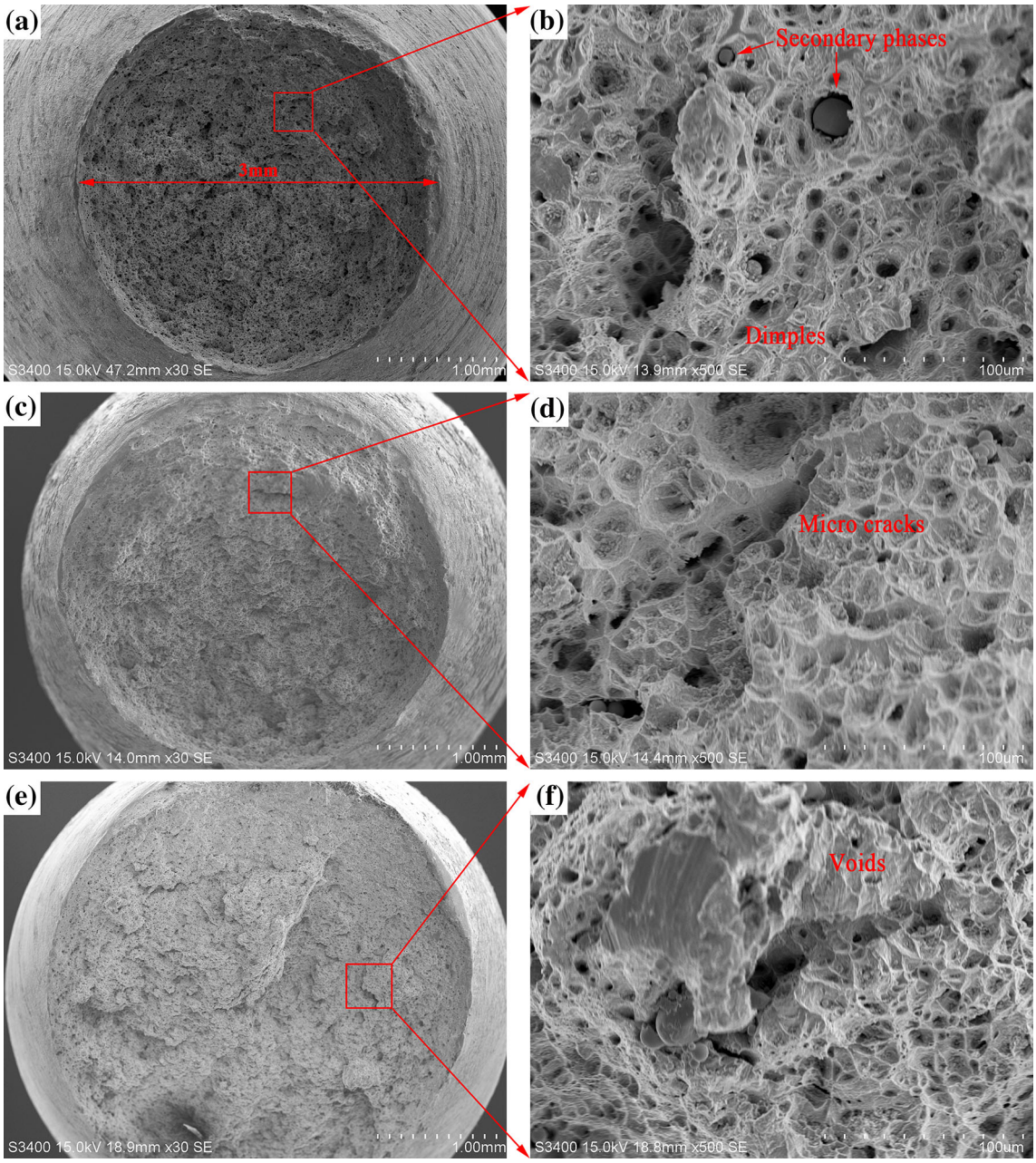

Fig. 6 Fracture morphologies of crept specimen with different applied stresses: (a, b) 180 MPa; (c, d) 160 MPa; (e, f) 140 MPa; (g, h) 120 MPa and (i, j) 110 MPa

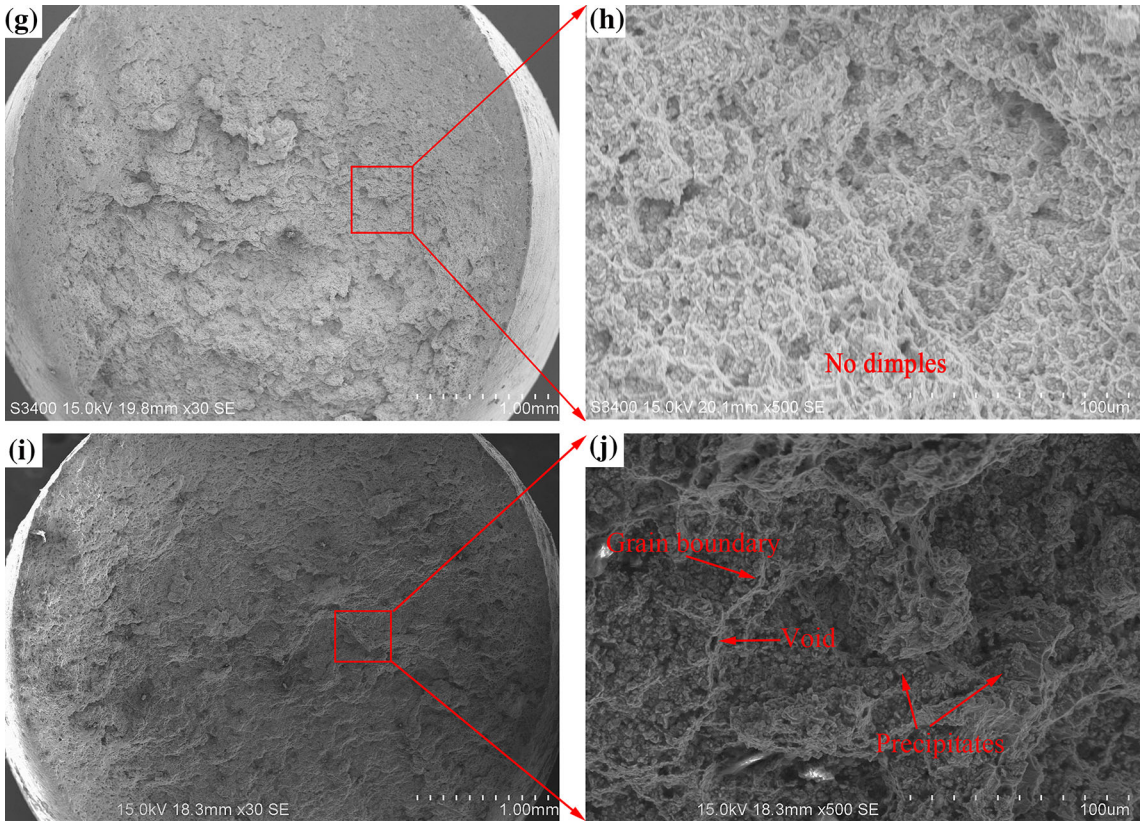

Fig. 6 continued

This may be caused by three main effects. Firstly, the undissolved carbides in FGHAZ are apt to grow and become coarse, which would stimulate the nucleation and growth of creep voids (Ref 9). Secondly, a fine grain size is beneficial to the tempering of microstructure and dynamic recovery processes during the creep exposure at high temperature and low stress. Thus, creep resistance in FGHAZ is the lowest in the T92 side. Thirdly, the multiaxial stress state originating from the constraint effect in the HAZ region with lower creep strength surrounded by the regions with higher creep strength (BM, CGHAZ) would accelerate the nucleation and growth of creep cavities (Ref 30-32).

4. Conclusion

1. Mechanical properties of T92/S30432 dissimilar steels welded joints at room temperature meet the requirements specified in the standards, among which the S30432 BM exhibits the lowest strength. And the weld seam part presents the lowest hardness.
2. The HAZ of martensitic T92 part in the dissimilar welds between T92 and S30432 steels consists of coarse- and fine-grained part due to the austenite-to-martensite phase transformation and the different peak temperatures of welding thermal cycle. In contrast, without the martensite transformation, the HAZ microstructure of the austenitic S30432 side does not exhibit the HAZ subregion and is exclusively formed of coarsened polygonal grains caused by welding heat input compared with the microstructure of S30432 BM.
3. During crept at 625 °C, the creep deformation and fracture behavior of T92/S30432 dissimilar weld joint are controlled by its martensitic T92 part due to the Ni-based filler metal employed.
4. The fracture positions of the crept dissimilar welded joints change with the applied stresses. As the applied stress over than 140 MPa, the failure occurs in BM of T92 steel, which exhibited the ductility facture controlled by plastic deformation and characterized by dimples and surface necking. While as the applied stress decreases <140 MPa, the fracture model of dissimilar welded joint is occurred in FGHAZ of T92, identified to be intergranular brittle fracture induced by the nucleation, growth and coalescence of creep voids.
5. The failure in FGHAZ at T92 side under low stress is mainly related to the undissolved carbides of FGHAZ caused by the welding thermal cycle, the fine grain size and the constraint effect induced by creep deformation inconsistent in this zone.

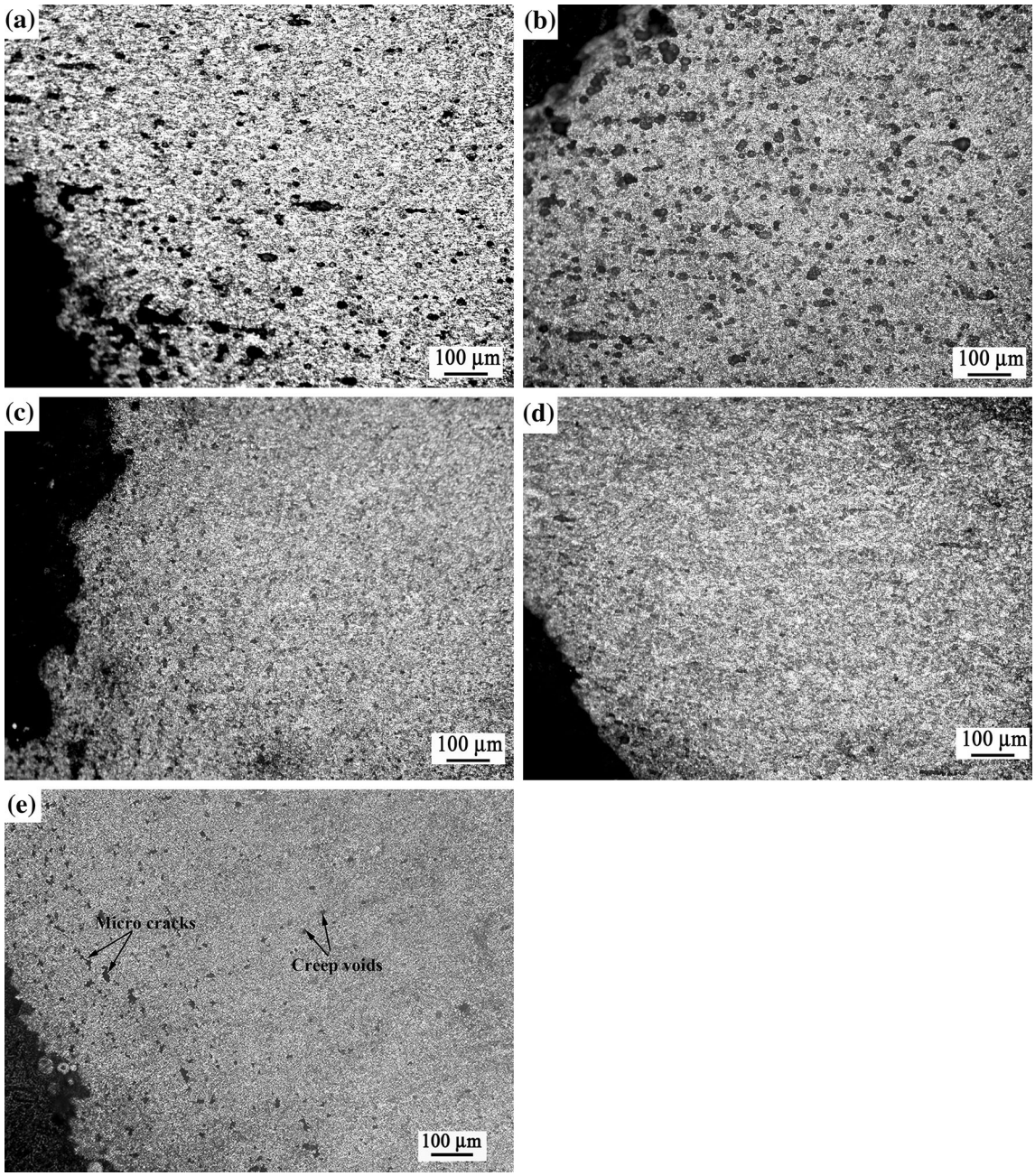

Fig. 7 Variation of fracture microstructures on the dissimilar welded joint crept under different applied stresses: (a) 180 MPa, (b) 160 MPa, (c) 140 MPa, (d) 120 MPa and (e) 110 MPa

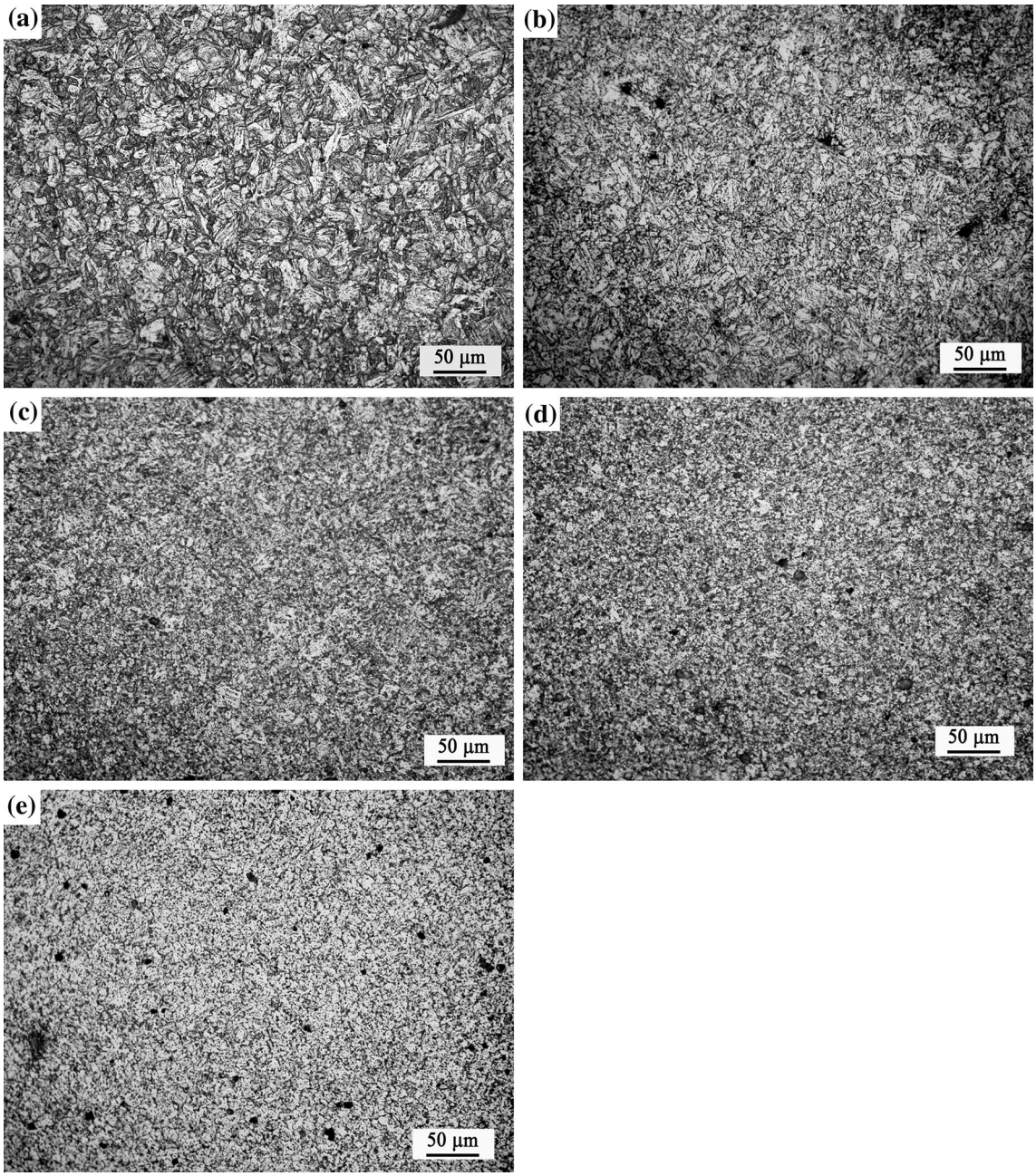

Fig. 8 Microstructure evolution in FGHAZ on T92 side crept under different applied stresses: (a) 180 MPa, (b) 160 MPa, (c) 140 MPa, (d) 120 MPa and (e) 110 MPa

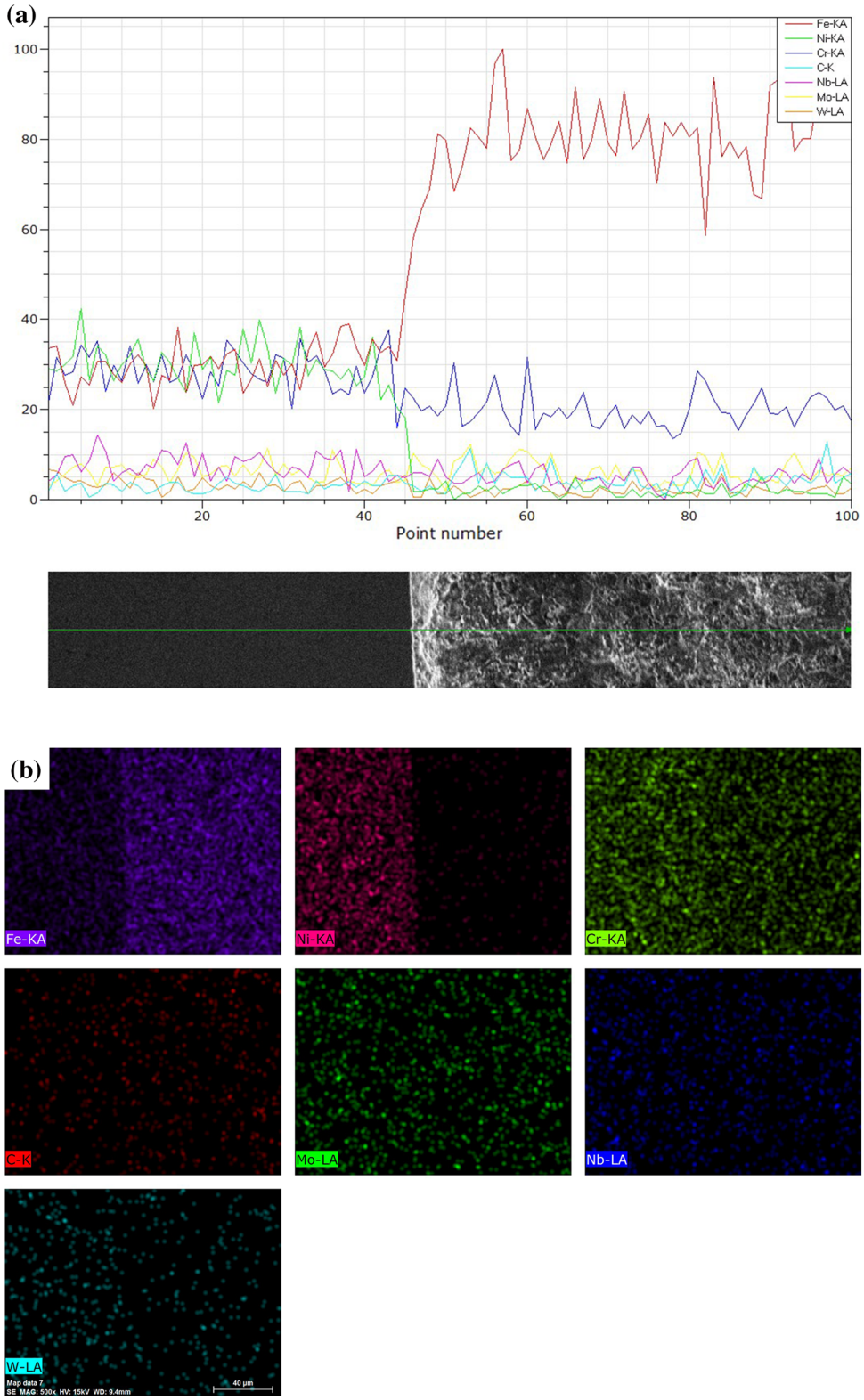

Fig. 9 Element distribution across the interface between HAZ of T92 and Ni-based WM: (a) line scan and (b) map scan

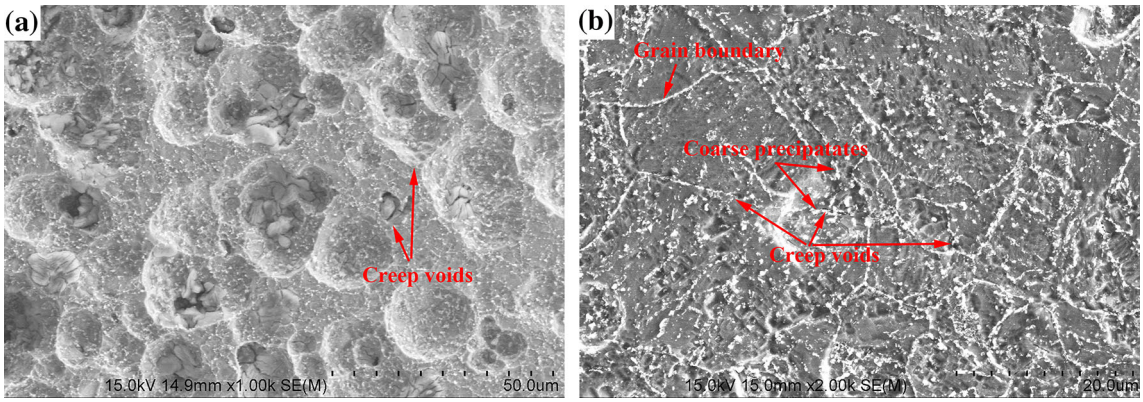

Fig. 10 SEM microstructure of FGHAZ in the specimen crept at 110 MPa

Acknowledgments

This research work was financially supported by Project of National Natural Science Foundation of China (Grant No. 51505328), Key Project in the Science and Technology Pillar Program of Tianjin (Grant No. 11ZCKFGX03000) and Distinguished-Reserved Academic Program of Tianjin University.

References

1. G. Cau, V. Tola, and P. Deiana, Comparative performance assessment of USC and IGCC power plants integrated with CO_2 capture systems, *Fuel*, 2014, **116**, p 820–833
2. B.N. Popov, X. Li, G. Liu, and J.-W. Lee, Power source research at USC: development of advanced electrocatalysts for polymer electrolyte membrane fuel cells, *Int. J. Hydrogen Energy*, 2011, **36**, p 1794–1802
3. T.-U. Kern, M. Staubli, and B. Scarlin, The European efforts in material development for 650°C USC power plants—COST522, *ISIJ Int.*, 2002, **42**, p 1515–1519
4. S.A. David, J.A. Siefert, and Z. Feng, Welding and weldability of candidate ferritic alloys for future advanced ultrasupercritical fossil power plants, *Sci. Technol. Weld. Join.*, 2013, **18**, p 631–651
5. K.-S. Park, D.-S. Bae, S.-K. Lee, G.-H. Lee, J.-H. Kim, and T. Endo, Creep modeling for life evaluation and strengthening mechanism of tungsten alloyed 9–12 % Cr steels, *Met. Mater. Int.*, 2006, **12**, p 385–391
6. V. Knezevic, G. Sauthoff, J. Vilk, G. Inden, A. Schneider, R. Agamennone et al., Martensitic/ferritic super heat-resistant 650 °C steels—Design and testing of model alloys, *ISIJ Int.*, 2002, **42**, p 1505–1514
7. J. Cao, Y. Gong, K. Zhu, Z.-G. Yang, X.-M. Luo, and F.-M. Gu, Microstructure and mechanical properties of dissimilar materials joints between T92 martensitic and S304H austenitic steels, *Mater. Des.*, 2011, **32**, p 2763–2770
8. Kim B-j, Kim H-j, and Lim B-s, Creep-fatigue damage and life prediction in P92 alloy by focused ultrasound measurements, *Met. Mater. Int.*, 2008, **14**, p 391–395
9. J. An, H. Jing, G. Xiao, L. Zhao, and L. Xu, Analysis of the creep behavior of P92 steel welded joint, *J. Mater. Eng. Perform.*, 2010, **20**, p 1474–1480
10. G. Lewis and K.M. Shaw, Creep constitutive model and component lifetime estimation: the case of niobium-modified 9Cr–1Mo steel weldments, *J. Mater. Eng. Perform.*, 2010, **20**, p 1310–1314
11. Y. Gao, C. Zhang, X. Xiong, Z. Zheng, and M. Zhu, Intergranular corrosion susceptibility of a novel Super304H stainless steel, *Eng. Fail. Anal.*, 2012, **24**, p 26–32
12. C. Chi, H. Hu, J. Dong, W. Liu, S. Cheng, Z. Liu, et al., The precipitation strengthening behavior of Cu-rich phase in Nb contained advanced Fe–Cr–Ni type austenitic heat resistant steel for USC power plant application, *Prog. Nat. Sci.*, 2012, **22**, p 175–185
13. J.A. Siefert, J.P. Shingledecker, J.N. DuPont, S.A. David, Weldability and weld performance of candidate nickel based superalloys for advanced ultrasupercritical fossil power plants. *Sci. Technol. Weld. Join.*, 2014, **19**, p 271–294
14. H. Osman, A. Borhana, and M.N. Tamin, Material parameters for creep rupture of austenitic stainless steel foils, *J. Mater. Eng. Perform.*, 2014, **23**, p 2858–2863
15. H.P. Buchkremer, P.J. Ennis, and D. Stöver, Manufacture and stress rupture properties of hipped austenitic–ferritic transition joints, *J. Mater. Process. Technol.*, 1999, **92–93**, p 368–370
16. J.P. Shingledecker and G.M. Pharr, Testing and analysis of full-scale creep-rupture experiments on inconel alloy 740 cold-formed tubing, *J. Mater. Eng. Perform.*, 2012, **22**, p 454–462
17. G. Chen, Q. Zhang, J. Liu, J. Wang, X. Yu, J. Hua et al., Microstructures and mechanical properties of T92/Super304H dissimilar steel weld joints after high-temperature ageing, *Mater. Des.*, 2013, **44**, p 469–475
18. L. Zhao, J. Liang, Q. Zhong, C. Yang, B. Sun, and J. Du, Numerical simulation on the effect of welding parameters on welding residual stresses in T92/S30432 dissimilar welded pipe, *Adv. Eng. Softw.*, 2014, **68**, p 70–79
19. R.D. Nicholson and J.A. Williams, Failure and deformation modes in heavy section dissimilar welds subjected to accelerated thermal cycle: creep loading, *Int. J. Press. Vessel. Pip.*, 1985, **20**, p 239–274
20. J.D. Parker and G.C. Stratford, The high-temperature performance of nickel-based transition joints: I. Deformation behaviour, *Mater. Sci. Eng. A*, 2001, **299**, p 164–173
21. J.D. Parker and G.C. Stratford, The high-temperature performance of nickel-based transition joints: II. Fracture behaviour, *Mater. Sci. Eng. A*, 2001, **299**, p 174–184
22. P. Parameswaran and K. Laha, Role of microstructure on creep rupture behaviour of similar and dissimilar joints of modified 9Cr–1Mo steel, *Procedia Eng.*, 2013, **55**, p 438–442
23. K. Laha, S. Latha, K.B.S. Rao, S.L. Mannan, and D.H. Sastry, Comparison of creep behaviour of 2.25Cr–1Mo/9Cr–1Mo dissimilar weld joint with its base and weld metals, *Mater. Sci. Technol.*, 2001, **17**, p 1265–1272
24. L. Zhao, H. Jing, L. Xu, J. An, G. Xiao, D. Xu et al., Investigation on mechanism of type IV cracking in P92 steel at 650 °C, *J. Mater. Res.*, 2011, **26**, p 934–943
25. K. Shinozaki, D. Li, H. Kuroki, H. Harada, K. Ohishi, and T. Sato, Observation of type IV cracking in welded joints of high chromium ferritic heat resistant steels, *Sci. Technol. Weld. Join.*, 2003, **8**, p 289–295
26. H. Tezuka and T. Sakurai, A trigger of type IV damage and a new heat treatment procedure to suppress it. Microstructural investigations of long-term ex-service Cr–Mo steel pipe elbows, *Int. J. Press. Vessel. Pip.*, 2005, **82**, p 165–174
27. K. Maruyama, K. Sawada, and K. Jun-Ichi, Strengthening mechanisms of creep resistant tempered martensitic steel, *ISIJ Int.*, 2001, **41**, p 641–653
28. J. Sopoušek and R. Foret, More sophisticated thermodynamic designs of welds between dissimilar steels, *Sci. Technol. Weld. Join.*, 2008, **13**, p 17–24

29. L. Falat, M. Svoboda, A. Výrostková, I. Petryshynets, and M. Sopko, Microstructure and creep characteristics of dissimilar T91/TP316H martensitic/austenitic welded joint with Ni-based weld metal, *Mater. Charact.*, 2012, **72**, p 15–23
30. K. Sawada, H. Hongo, T. Watanabe, and M. Tabuchi, Analysis of the microstructure near the crack tip of ASME Gr.92 steel after creep crack growth, *Mater. Charact.*, 2010, **61**, p 1097–1102
31. L. Zhao, H. Jing, L. Xu, J. An, and G. Xiao, Numerical investigation of factors affecting creep damage accumulation in ASME P92 steel welded joint, *Mater. Des.*, 2012, **34**, p 566–575
32. D. Li and K. Shinozaki, Simulation of role of precipitate in creep void occurrence in heat affected zone of high Cr ferritic heat resistant steels, *Sci. Technol. Weld. Join.*, 2005, **10**, p 544–549